Pergamon

Geochimica et Cosmochimica Acta, Vol. 68, No. 5, pp. 969–983, 2004

0016-7037/04 $30.00 + .00

doi:10.1016/j.gca.2003.07.013

Speciation and characterization of arsenic in gold ores and cyanidation tailings using X-ray absorption spectroscopy

DOGAN PAKTUNC,[1,*] ANDREA FOSTER,[2] STEVE HEALD,[3] and GILLES LAFLAMME[1]

[1]CANMET, Mining and Mineral Sciences Laboratories, 555 Booth Street, Ottawa, ON, K1A 0G1, Canada
[2]USGS Mineral Resources Division, 345 Middlefield Rd., Menlo Park, CA 94025, USA
[3]Advanced Photon Source, 9700 S. Cass Ave., Argonne, IL 60439, USA

(*Received April* 17, 2003; *accepted in revised form July* 28, 2003)

Abstract—The knowledge of mineralogy and molecular structure of As is needed to better understand the stability of As in wastes resulting from processing of gold ores. In this study, optical microscopy, scanning electron microscopy, electron microprobe, X-ray diffraction and X-ray absorption fine structure (XAFS) spectroscopy (including both XANES and EXAFS regimes) were employed to determine the mineralogical composition and local coordination environment of As in gold ores and process tailings from bench-scale tests designed to mimic a common plant practice. Arsenic-bearing minerals identified in the ores and tailings include iron (III) oxyhydroxides, scorodite ($FeAsO_4 \cdot 2H_2O$), ferric arsenates, arseniosiderite ($Ca_2Fe_3(AsO_4)_3O_2 \cdot 3H_2O$), Ca-Fe arsenates, pharmacosiderite ($KFe_4(AsO_4)_3(OH)_4 \cdot 6–7H_2O$), jarosite ($K_2Fe_6(SO_4)_4(OH)_{12}$) and arsenopyrite (FeAsS). Iron (III) oxyhydroxides contain variable levels of As from trace to about 22 wt% and Ca up to approximately 9 wt%.

Finely ground ore and tailings samples were examined by bulk XAFS and selected mineral grains were analyzed by microfocused XAFS (micro-EXAFS) spectroscopy to reconcile the ambiguities of multiple As sources in the complex bulk EXAFS spectra. XANES spectra indicated that As occurs as As^{5+} in all the samples. Micro-EXAFS spectra of individual iron (III) oxyhydroxide grains with varying As concentrations point to inner-sphere bidentate-binuclear arsenate complexes as the predominant form of As. There are indications for the presence of a second Fe shell corresponding to bidentate-mononuclear arrangement. Iron (III) oxyhydroxides with high As concentrations corresponding to maximum adsorption densities probably occur as nanoparticles. The discovery of Ca atoms around As in iron (III) oxyhydroxides at interatomic distances of 4.14–4.17 Å and the coordination numbers suggest the formation of arseniosiderite-like nanoclusters by coprecipitation rather than simple adsorption of Ca onto iron (III) oxyhydroxides. Correlation of Ca with As in iron (III) oxyhydroxides as determined by electron microprobe analysis supports the coprecipitate origin for the presence of Ca in iron (III) oxyhydroxides.

The samples containing higher abundances of ferric arsenates released higher As concentrations during the cyanidation tests. The presence of highly soluble ferric arsenates and Ca-Fe arsenates, and relatively unstable iron (III) oxyhydroxides with Fe/As molar ratios of less than 4 in the ore and process tailings suggests that not only the tailings in the impoundment will continue to release As, but also there is the potential for mobilization of As from the natural sources such as the unmined ore.

1. INTRODUCTION

Recent epidemiological findings on the toxicological effects of arsenic (As) in drinking water in Bangladesh and India have prompted drastic revision of the drinking water guidelines and renewed interests on As research. The source of As in drinking water of Bangladesh is natural, but the toxic As concentrations are resulting from human activity (e.g., Harvey et al., 2002). Tailings resulting from mining and milling operations constitute one of the important anthropogenic sources of As in the environment. Effluent discharges containing As have the potential to adversely affect the water quality of receiving waters. Accordingly, current effluent guidelines are being reconsidered by the regulatory bodies.

The Ketza River mine is a former gold mine located in south-central Yukon, Canada. The gold mineralization, which was discovered in 1954, is made up of two types of ore bodies: 189605 tons of sulfide ore grading 11.3 g/t Au and 495800 tons of oxide ore grading 18 g/t Au. During a brief period from 1988 to 1990, the mine produced over 2.8 tons (100000 oz) of gold through a 320 t/d mill employing conventional carbon-in-pulp (CIP) cyanidation leach. Following the extraction of the gold, residual free cyanide in the tailings was destroyed by the use of the INCO SO_2/air process (Devuyst et al., 1989). Approximately 310000 tons of tailings were produced during the 2-yr operation and they were deposited in a tailings impoundment under partial water cover. The tailings contain on average 4 to 7 wt% As. Arsenic in the excess reclaim water from the tailings pond was reduced to 0.08 mg/L by a process involving ferric arsenate precipitation followed by flocculation and solids removal before discharge through a polishing pond to the creek (T.W. Higgs, private communication).

There are concerns over the mobilization of As from the Ketza River mine tailings impoundment. Column-leaching studies by the Environmental Protection Branch of Environment Canada in Yukon (Soprovich, 2000) on the tailings indicated As releases that were considerably higher than what was deemed to be environmentally acceptable limits for mine effluents (i.e., greater than the maximum authorized monthly

* Author to whom correspondence should be addressed (dpaktunc@NRCan.gc.ca).

Table 1. Bulk chemistry of the ore and tailings samples (wt%).[a]

	18	18-CIP	18-SO2	20	20-CIP	20-SO2	22	22-CIP	22-SO2	ORE
SiO_2	17.76	16.47	17.54	11.77	10.70	10.05	9.41	7.92	7.49	9.20
TiO_2	0.05	0.04	0.05	0.04	0.04	0.04	0.02	0.02	0.17	0.03
Al_2O_3	2.68	2.83	2.83	1.89	2.27	2.27	0.81	0.89	0.94	0.98
Fe_2O_3	43.25	39.89	43.89	44.61	41.32	40.46	67.20	67.34	64.62	68.20*
FeO	0.90	3.60	0.00	0.90	0.00	0.77	5.01	0.00	2.96	na
MnO	0.26	0.26	0.26	0.19	0.21	0.21	1.65	1.94	1.94	1.86
MgO	1.04	1.09	1.08	0.83	0.83	0.81	0.60	0.66	0.65	0.70
CaO	9.23	10.07	10.77	15.81	17.35	17.49	1.32	2.66	2.80	1.76
As_2O_5	5.16	6.38	6.24	3.46	4.28	4.21	4.67	6.55	6.64	6.12
K_2O	0.45	0.52	0.52	0.30	0.42	0.40	0.16	0.19	0.19	0.20
Na_2O	nd	nd	nd	nd	nd	nd	nd	nd	nd	0.09
CO_2	7.26	6.01	5.98	12.00	11.01	9.79	0.20	nd	nd	na
$S_{(s)}$	0.58	0.23	0.42	0.13	0.05	0.07	0.21	0.00	0.10	0.32*
SO_4	0.24	1.25	2.10	0.12	0.62	2.22	0.36	1.38	2.17	na
Total	88.85	88.65	91.68	92.04	89.10	88.78	91.61	89.53	90.66	89.47

[a] $S_{(s)}$: sulfide sulfur after subtracting sulfur tied to SO_4; na: not analyzed; nd: not determined (i.e. below detection limit); * total Fe as Fe_2O_3 and total S.

mean concentration of 0.5 mg/L As). It was not known to what extent, if any, the milling process might have played a role in As distribution and how it contributed to the leachability of the arsenic. Earlier studies indicated that As mineralogy of the ore and tailings is complex (Paktunc et al., 1996, 1998). This necessitated detailed speciation and characterization studies at the molecular scale to better determine the form, nature and distribution of As in the ore and process tailings. Along with the knowledge of geochemical processes controlling As mobility, the source characteristics will help to develop a better understanding of As concentrations in the effluents.

Accordingly, the objectives of this study were (1) to study the mineralogical make-up of the ores and process tailings, (2) to study the molecular-scale speciation of As in the ore and process tailings, and (3) to determine the stability of the As-bearing minerals and compounds.

The results will provide basic data for the development of options for the long-term (environmentally acceptable) containment of the tailings by strengthening the arguments on the prediction of As mobility under varying environmental conditions. The results can be applicable elsewhere since processing of gold ores often result in tailings and effluents containing high As concentrations. This study has also important bearings on the controversial subject of long-term stability of ferric arsenate and/or arsenical ferrihydrite precipitates commonly used by the industry to control As in metallurgical processing.

2. MATERIALS AND METHODS

2.1. Samples and Experimental Work

Four types of oxide ore were selected for this study. The ore sample, labeled as ORE, is a composite made from the diamond drill cores of the oxidized ore. The other ore samples, labeled as 18, 20 and 22, are also composites, prepared by mixing rock fragments and fines taken randomly from the ore dump, ore chute, grizzly crusher and the conveyor belt with the intend to resemble the feed ore processed during milling. Although it is not known how well these four samples would represent the entire oxide ore body, the chemical variability shown by the composite samples (Table 1) cover the bulk sample analysis of the oxide ore as reported in a 1986 company report.

Bench-scale cyanidation tests were carried out to simulate plant practice at the Ketza River mill (Paktunc et al., 2000). The ore samples, 18, 20 and 22 were ground to approximately 70% passing 200 mesh (i.e., <63 μm) and split in half after obtaining subsamples for mineralogical, chemical and spectroscopic studies. The ore samples weighing 2 kg, were placed in a glass reactor and mixed with 3 L distilled water. The leaching tests were conducted for 48 h at a constant pH of 10.5 maintained with lime (CaO) addition and constant dissolved oxygen concentration of 7.5 mg/L. Cyanide leaching involved 2 g NaCN with a retention time of 48 h. Gold was removed by adsorption on activated carbon granules. The slurries, which resulted from the cyanidation-CIP gold extraction tests and made of approximately 2 kg of ore and 3 L of solution, were batch-processed to destroy the residual cyanide by using the INCO SO_2/air process. The INCO process uses a gaseous mixture of air and SO_2 to oxidize cyanide to cyanate, which then decomposes to produce ammonia and CO_2. The slurries were contacted in a 4-L glass reaction vessel with a mixture of air and SO_2 gas while applying vigorous mechanical agitation. Copper was added at the beginning of each experiment as a catalyst. The pH, which tends to drop during the experiment because of the generation of sulfuric acid, was kept alkaline by lime addition. The experiment was stopped when the free cyanide concentration dropped below 25 mg/L. At the end of each experiment, the pulp was filtered to separate the solids from the solution. The solution samples were analyzed for a range of elements and ions by inductively-coupled plasma atomic emission spectrometry and ion chromatography techniques (Table 2). The residual solid samples after cyanidation and SO_2/air destruction were dried at room temperature and labeled as 18-CIP, 20-CIP and 22-CIP, and 18-SO2, 20-SO2 and 22-SO2, respectively.

2.2. Mineralogy

Epoxy mounts, measuring 30 mm in diameter and $\sim$10 mm in thickness, from the ore samples and their tailings after cyanidation tests were prepared and polished. The samples were examined under optical microscope, scanning electron

Table 2. Solution chemistry following cyanidation (CIP) and SO_2/air process.

	18-CIP	18-SO2	20-CIP	20-SO2	22-CIP	22-SO2
pH	10.5	9.5	10.5	8.2	10.5	8.5
Alkalinity (mg/L)	172	34	340	33	160	57
SO_4 (mg/L)	1382	1414	736	2643	1700	2421
As (mg/L)	6.6	11.4	4.7	2.4	2.8	1.1
Ca (mg/L)	577	471	272	498	514	552
Fe (mg/L)	0.26	0.3	1.2	nd[a]	1.3	0.1
Mg (mg/L)	0.99	13	0.5	32	1.7	27

[a] nd: not detected.

microscope and electron microprobe. Mineral identifications in scanning electron microscope examinations were made by energy-dispersive X-ray microanalysis and the grey levels in backscattered electron images. Quantitative electron microprobe analyses were performed by wavelength dispersion spectrometry (WDS) on JEOL 733 and JEOL 8900 microanalyzers, operated at 20 kV with a beam current of 20 nA (cup reading). The following X-ray lines and standards were used: Fe$K\alpha$ (synthetic Fe_2O_3), Mn$K\alpha$ (synthetic $MnTiO_3$), Ca$K\alpha$ (sphene), Al$K\alpha$ (synthetic $MgAl_2O_4$), As$L\alpha$ (synthetic InAs), Si$K\alpha$ (wollastonite) and S$K\alpha$ (synthetic $PbSO_4$). Counting time was on the order of 40 s for the minor and trace elements, and raw data corrections for atomic number, absorption and fluorescence effects (ZAF) were applied. The samples were also examined using a Rigaku rotating anode X-ray powder diffractometer with Cu$K\alpha$ radiation at 55 kV, 180 mA, step-scan 0.04°, scan rate at 4° per minute in 2θ. The samples were finely ground to less than ~44 μm (−325 mesh) and packed on Teflon covered aluminum sample holders for X-ray powder diffraction analysis. A selected number of individual mineral grains, analyzed by electron microprobe, were extracted from the polished sections and analyzed by Debye-Scherrer camera to collect X-ray powder diffraction patterns to confirm mineral identification. The bulk samples were analyzed by a combination of atomic absorption and inductively-coupled plasma atomic emission spectrometry techniques to determine the concentrations of Si, Ti, Al, total Fe, Mn, Mg, Ca, Na, K and As. In addition, the samples were analyzed for total S and C by a LECO combustion apparatus. The CO_2 determinations were made by LECO following 20% HCl leach and SO_4 by ion chromatography following Na carbonate leach. Ferrous iron determinations were made by spectrophotometric analysis and ferric iron by difference from total Fe.

2.3. X-Ray Absorption Fine Structure (XAFS) Spectroscopy

The XAFS experiments were carried out at the Stanford Synchrotron Radiation Laboratory (SSRL), Stanford University, CA, USA on wiggler beamline 4–3 and bending magnet beamline 2–3. All the samples listed on Table 1 (both treated and untreated) were analyzed. Air-dried samples were finely ground in an agate mortar to achieve particle sizes of about several μm across and mixed with boron nitride to dilute the concentrated samples to ~1 wt% As and less for optimization of absorption by the sample (i.e., produce an absorption length, μx, of ~1 where μ is the mass absorption coefficient of the sample and x is the sample thickness) and loaded into Teflon holders with Mylar windows. Silicon (111) and (220) double-crystal monochromators with 1 mm vertical slits were used. The monochromator was detuned to 50% to eliminate harmonic contributions. A thin As metal (foil) was placed between the second and third ionization chambers for energy calibration at the inflection point of 11867 eV. Nitrogen gas was used in the first and second ionization chambers, argon in the third and xenon or argon gas was used in the fourth detector (fluorescence). The XAFS spectra were collected at room temperature in the fluorescence mode using a Lytle detector. XANES spectra were obtained by scanning the monochromator at 0.2 eV steps over the edge region and the EXAFS (extended XAFS regime) spectra at 1.8 to 6.2 eV steps over the EXAFS region. Acquisition time was 3 to 5 min for XANES analysis and approximately 2.5 h for EXAFS analysis. At least 4 individual XAFS (XANES + EXAFS) scans were collected for each sample for statistical purposes and to increase signal-to-noise ratio in the EXAFS region.

Micro-EXAFS experiments were carried out at the PNC-CAT's undulator beamline (20-ID) of the Advanced Photon Source (APS), Argonne, IL, USA. A Si(111) monochromator and Kirkpatrick-Baez mirrors were used. The Kirkpatrick-Baez mirrors reduce the harmonics and enable focusing the beam to a small spot size. A beam size of approximately 5 μm (i.e., 6.8 μm vertical and 4.5 μm horizontal dimension) was used. A range of iron (III) oxyhydroxide grains with variable As concentrations and arsenate mineral grains in three polished sections analyzed by electron microprobe and representing samples 18-CIP, 20 and 22-CIP were marked for XAFS analysis. Larger mineral grains (i.e., ~> 60 μm) marked on polished sections were located under the beam with the help of a binocular microscope. Smaller mineral grains were placed under the beam by scanning the area at 5 to 6 μm steps and producing As, Ca and Fe fluorescence maps of the area. Micro-EXAFS spectra were collected from the center of mineral grains in fluorescence mode using an ion chamber detector and a 13-element Ge detector to monitor the intensity of As $K\alpha$ X-rays emitted from the sample. The first ionization chamber located between the mirrors and the sample was filled with nitrogen and the fluorescent detector by argon. On average, four micro-EXAFS scans were collected on each mineral grain.

Data reduction was accomplished using EXAFSPAK (George and Pickering, 1995), and IFEFFIT (Newville, 2001). Data reduction involved the subtraction of a polynomial preedge, followed by removal of the postedge background by a Victoreen-spline function anchored on the low-energy side at 11885 eV. The XAFS spectra were weighted by k^3 to amplify the oscillations at high k and Fourier transformed (Fast Fourier transform) into R-space. An assessment of the presence of systematic noise and random noise was made on the Fourier-transformed XAFS spectra following Stern et al. (1995) and Stern (2001) by analyzing individual scans in addition to the averaged spectra. EXAFS data analysis was performed with theoretical phase and amplitude functions generated in FEFF7 (Zabinsky et al., 1995) from scorodite ($FeAsO_4 \cdot 2H_2O$) and rauenthalite [$Ca_3(AsO_4)_2 \cdot 10H_2O$]. A fixed value of 0.85 was used for the amplitude reduction factor (S_0^2). The Marquardt algorithm in EXAFSPAK was used in curve fitting and the

Table 3. X-ray diffraction lines by Debye-Scherrer camera from a representative set of individual mineral grains.[a]

Goethite										Scorodite					Arseniosiderite						
Reference			A1		A2		A3		A4	Reference			A5		Reference			A6		A7	
d(Å)	(hkl)	I	d(Å)	I	d(Å)	I	d(Å)	I	d(Å)	I	d(Å)	(hkl)	I	d(Å)	I	d(Å)	(hkl)	I	d(Å)	I	d(Å)	I
4.183	(110)	100	[4.18]		4.18	s	4.17	s	[4.18]		5.609	(111)	80	5.60	s	3.280	(213)	40	3.30	m	3.30	
2.693	(130)	35	2.71	m	2.69		2.70		2.68	m	4.472	(200)	100	4.46	s	3.220	(−342)	40	3.25	m	3.20	
2.450	(111)	50	2.45	m	2.44	m	2.45	m	2.45	m	3.178	(212)	90	3.19	s	2.945	(600)	50	2.95		2.95	m
2.253	(121)	14	2.27				2.25		2.25		3.060	(131)	45	3.05		2.772	(−204)	80	2.77	s	2.75	s
2.190	(140)	18	2.20				2.18		2.19		2.999	(113)	35	2.98		2.622	(460)	30	2.62		2.65	m
1.802	(211)	6							1.80		2.682	(203)	25	2.67		2.522	(640)	20	2.52		2.55	
1.719	(221)	20	1.72	m	1.71		1.71	m	1.72	m	2.596	(213)	35	2.59	m	2.491	(−404)	20	2.48			
1.564	(151)	10	1.57				1.56		1.56		2.501	(321)	25	2.50		2.213	(182)	40	2.21		2.23	
1.509	(002)	8	1.51		1.51		1.50		1.51		2.044	(402)	4	2.03		1.891	(911)	20	1.90		1.91	
1.454	(061)	5	1.45						1.45		2.005	(412)	13	2.00		1.857	(193)	10	1.87		1.80	
																1.770	(1000)	20	1.77		1.77	
																1.643	(791)	40	1.64	m	1.64	m

[a] Goethite reference: PDF#29-0713; scorodite reference: PDF#37-0468; arseniosiderite reference: PDF#26-1002; I: intensity; s: strong; m: medium; d values in brackets represent obscured or broadened lines due to darkening of the pinhole; see Table 4 for chemical compositions for the mineral grains.

fitting space was k. To ensure that the fit parameters did not result from a local or false minimum, the fitting was repeated by using different initial values for the fitting parameters. Proportions of the As-bearing minerals were determined by solving a simultaneous set of mass balance equations:

$$\chi_i^{bulk}(k) \cdot k^3 = \sum_{j=1}^{m} \chi_i^m(k) \cdot k^3 \cdot q^m$$

where $\chi(k) \cdot k^3$ is the k^3-weighted bulk EXAFS, m is number of minerals or compounds, q is the fraction of As atoms in mineral m and i is the number of experimental data points. Because the system of linear equations is overdetermined (i.e., $i \gg m$), Gaussian elimination and multiple regression techniques were employed to reduce the solutions. The fractions (q^m) should ideally sum to 1 for m number of minerals, but this is not constrained to allow another quantity whereby the quality of the fit can be judged. A computer program, LSFitXAFS was written for this purpose and is provided as an Electronic Annex (Elsevier Website, Science Direct) to this paper (also available from the principal author upon request). The goodness-of-fit parameters in EXAFS data analysis and background levels (i.e., systematic and random noise in Fourier-transformed XAFS spectra) were determined by this program as well.

3. RESULTS AND DISCUSSION

3.1. Mineralogical Composition

Iron (III) oxyhydroxides are the dominant species, forming more than one half of the mineral particles in all the samples studied. Goethite is the dominant iron (III) oxyhydroxide species as it is the only species positively identified by XRD (Table 3). Arsenopyrite (FeAsS), pyrite (FeS_2) and pyrrhotite ($Fe_{0.83-1}S$) occur in trace concentrations. Samples 18 and 20 consist of iron (III) oxyhydroxides, quartz (SiO_2), muscovite ($KAl_2(Si_3Al)O_{10}(OH,F)_2$), clinochlore ($(Mg, Fe)_5Al(Si_3Al)O_{10}(OH)_8$), calcite ($CaCO_3$), dolomite-($CaMg(CO_3)_2$), ankerite ($Ca(Fe, Mg)(CO_3)_2$), scorodite ($FeAsO_4 \cdot 2H_2O$), arseniosiderite ($Ca_2Fe_3(AsO_4)_3O_2 \cdot 3H_2O$), gypsum ($CaSO_4 \cdot 2H_2O$), jarosite ($K_2Fe_6(SO_4)_4(OH)_{12}$), pharmacosiderite ($KFe_4(AsO_4)_3(OH)_4 \cdot 6-7H_2O$), arsenopyrite, pyrite, pyrrhotite and gold (Au). Samples ORE and 22 consist of iron (III) oxyhydroxides, quartz, muscovite, grunerite ($(Fe, Mg)_7Si_8O_{22}(OH)_2$), magnetite ($Fe_3O_4$), scorodite, arseniosiderite, pharmacosiderite, jarosite, gypsum, arsenopyrite, pyrite and pyrrhotite. There are no apparent differences in the As mineralogy of the four ore samples and the mineralogical compositions of the tailings after the cyanidation and INCO SO_2/air processes are similar to those of their original counterparts.

Iron (III) oxyhydroxides occur mostly as discrete particles, but also as secondary reaction products on pyrite grains and as replacement products along the grain boundaries and microfractures in pyrite and arsenopyrite (Figs. 1a–c). Replacement is defined as the dissolution of one mineral and simultaneous deposition of another mineral in its place. Iron (III) oxyhydroxides that occur as discrete particles or as secondary reaction products on pyrite grains display zoning and colloform banding (Fig. 1d). Electron microprobe analyses indicate that iron (III) oxyhydroxides have variable and elevated levels of As and Ca (Table 4). In addition, some iron (III) oxyhydroxide particles contain trace to minor concentrations of Al, Si, Mn and S. Scorodite occurs as discrete particles, as fine-grained agglomerations and as replacement products after arsenopyrite. Scorodite may occur in association with As-bearing iron (III) oxyhydroxide, displaying a colloform texture and as enclosing anhedral fragments of pyrite. Electron microprobe analyses indicate that scorodite particles can contain up to ~2 wt% CaO (Table 4). Close association of iron (III) oxyhydroxides with variable levels of As and ferric arsenates in successive bands is suggestive of precipitation in close intervals. Ca-Fe arsenates (including arseniosiderite) occur as massive, compositionally zoned particles, leaf-like aggregates with radial growth textures (Fig. 2a,b), spheroidal aggregates and as replacement products of arsenopyrite

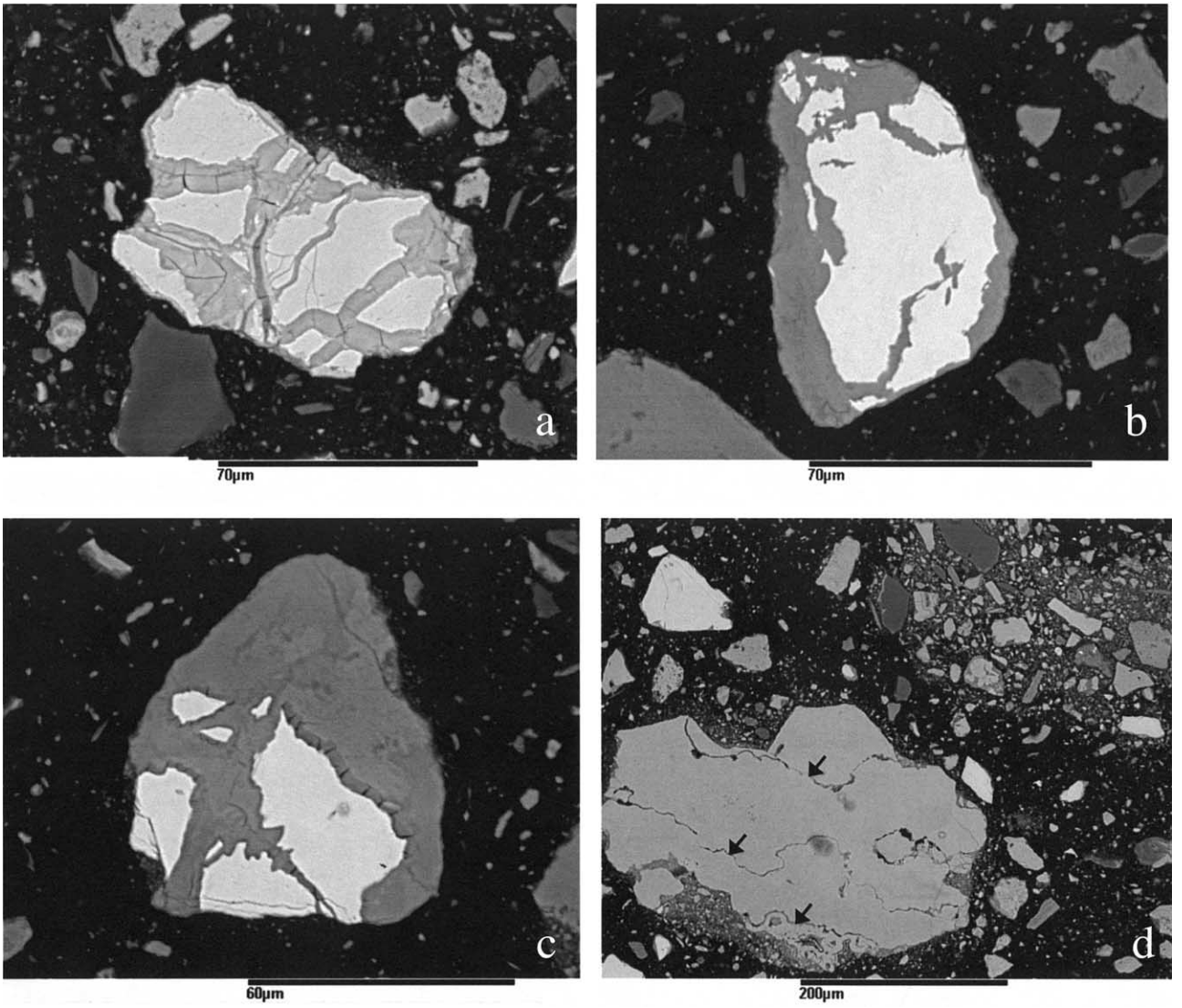

Fig. 1. Backscattered electron micrographs of (a) a pyrite particle (white) being replaced by secondary As-bearing iron (III) oxyhydroxide (light grey) along microfractures (sample 18); (b) arsenopyrite (white) replacement by arseniosiderite (grey) (sample 18); (c) relict arsenopyrite grains after replacement by scorodite (dark grey) and arseniosiderite (lighter grey) and Ca-Fe arsenate (dark grey rim with dehydration cracks around arsenopyrite) (sample 22); (d) a colloform banded (arrows) iron (III) oxyhydroxide particle (sample 22-SO2). Mineral identifications are based on energy-dispersive X-ray microanalysis or electron microprobe analysis.

and scorodite. In several samples, it was observed that scorodite is replaced by a Ca-Fe arsenate. Precipitation of arseniosiderite appears to postdate the Ca-Fe arsenate phase as evidenced by the occurrence of arseniosiderite around a Ca-Fe arsenate spheroid. Jarosite occurs as a heterogeneous phase with As concentrations varying from 0.7 to 8.5 wt% As_2O_5. Jarosite occurs in close association with arseniosiderite and iron (III) oxyhydroxides (Fig. 2c,d). Arsenopyrite occurs in minor to trace quantities in all samples as free and relict particles measuring less than ~150 μm. The relict arsenopyrite particles in scorodite, arseniosiderite, Fe-Ca arsenates, and As-bearing iron (III) oxyhydroxides would be protected from further oxidative dissolution by limiting the reaction to diffusion of reactants and products.

As shown on Figures 3 and 4, the chemical compositions of iron (III) oxyhydroxide and arsenate minerals, based on over 1300 electron microprobe analyses, are highly variable. On the Fe_2O_3 vs. As_2O_5 plot, iron (III) oxyhydroxides group in an array from goethite and ferrihydrite compositions pointing toward scorodite and Ca-Fe arsenate compositions. Main grouping is confined to Fe/As molar ratios of 9 and greater. The other grouping on the Fe_2O_3 vs. As_2O_5 plot is near scorodite and other arsenate mineral compositions. Eight goethite grains extracted from polished sections whose crystal structure was confirmed by X-ray diffraction (Debye-Scherrer) contain As_2O_5 and CaO ranging from 1.1 to 33.6 wt% and 0.3 to 11.2 wt%, respectively (Table 3). This places a lower limit of 1.6 on the Fe/As molar ratios of goethites. Theoretical Fe/As molar ratios of the common arsenate minerals are between 1 and 1.5. Thus, grains having Fe/As

Table 4. Representative electron microprobe analysis (wt%) of As-bearing iron (III) oxyhydroxides and arsenate minerals.[a]

Mineral	Fe_2O_3	As_2O_5	CaO	MnO	Al_2O_3	SiO_2	SO_3
Goethite	82.38	0.08	0.24	0.00	0.00	0.55	0.71
	80.11	1.13	0.34	0.02	0.04	1.53	0.09_{A1}
	79.80	2.37	0.80	0.11	0.15	1.31	0.08_{B1}
	78.49	2.97	0.82	0.33	0.64	1.26	0.07_{B2}
	77.05	3.35	1.42	0.06	0.69	0.72	0.17_{B3}
	79.80	3.41	1.04	0.16	0.22	0.93	0.49_{B4}
	75.07	5.13	1.23	0.03	1.15	0.99	0.03_{A2}
	74.75	6.04	1.44	0.00	0.61	1.09	0.05_{A3}
	76.54	6.14	1.78	0.00	0.17	0.14	0.16_{B5}
	70.50	7.70	2.30	0.11	0.35	0.43	0.29_{B6}
	69.56	9.61	3.58	0.00	0.75	0.10	0.56
	62.77	14.06	3.14	0.60	0.13	0.94	0.22
	46.55	19.84	5.39	0.73	0.26	1.77	1.29_{B7}
	50.75	23.34	8.34	0.00	0.06	1.30	0.41
	44.57	26.23	9.82	0.07	0.13	2.78	0.42_{B8}
	36.67	33.55	11.17	0.31	0.36	2.35	0.47_{A4}
Scorodite	38.53	47.46	0.23	0.00	0.58	0.00	0.49
	36.20	49.59	1.15	0.00	0.00	0.00	0.67_{A5}
	35.63	51.55	0.46	0.12	0.00	0.00	1.23
	36.20	53.45	0.03	0.01	0.00	0.00	0.22
	34.72	51.79	0.33	0.05	0.03	0.12	0.18_{B9}
	39.72	35.58	1.76	0.00	0.16	0.30	0.54_{B10}
Arseniosiderite	32.06	43.01	14.14	0.00	0.01	0.07	0.10
	31.83	43.14	14.65	0.01	0.02	0.14	0.02_{A6}
	31.22	41.91	14.29	0.01	0.02	0.18	0.03_{A7}
	35.81	39.57	12.47	0.03	0.04	0.34	0.09_{B11}
	33.22	42.06	13.50	0.44	0.57	1.24	0.21_{B12}
	32.07	41.29	14.29	0.51	0.10	0.57	0.00_{B13}
Yukonite	40.01	38.91	7.39	0.08	0.00	0.20	1.19
	36.08	43.01	8.21	0.67	0.06	0.28	0.45
Ca-Fe arsenate	40.19	31.24	11.54	0.05	0.05	2.11	0.32
	33.47	35.66	11.33	0.52	0.14	0.64	0.07
	33.13	38.58	11.81	0.10	0.01	0.55	0.03

[a] Mineral grains analyzed by Debye-Scherrer XRD (see Table 3): A1-A4: goethite; A5: scorodite; A6-A7: arseniosiderite. Mineral grains analysed by micro-EXAFS: B1: 20 #5; B2: 20-CIP#1A; B3: 20-CIP#110; B4: 20-CIP#15; B5: 18-CIP#8; B6: 18-CIP#B; B7: 20-CIP#17; B8: 20-CIP#23; B9: 18-CIP#C; B10: 18-CIP#D; B11: 20 #3; B12: 20-CIP#1X; B13: 20-CIP#22.

molar ratios greater than 1.5 are considered to be iron (III) oxyhydroxides in the data set.

The CaO levels in iron (III) oxyhydroxides vary from 0.03 to 12.7 wt% as a function of Fe_2O_3 and As_2O_5 concentrations (Fig. 4). Like As_2O_5, CaO variation correlates negatively with Fe_2O_3. On the CaO vs. As_2O_5 plot, iron (III) oxyhydroxides group in an array pointing toward arseniosiderite and yukonite compositions. The correlation coefficient of this grouping with 885 analyses is 0.91 and the average Ca/As molar ratio is 0.55. The highest Ca/As molar ratio is 0.67, which corresponds to arseniosiderite. The Ca/As ratio of the goethites identified by X-ray diffraction is 0.59. In other words, for every 2 Ca ions in iron (III) oxyhydroxide, there are 3 to 3.6 arsenate ions. This relationship does not support the view of Ca occurrence in iron (III) oxyhydroxides as adsorbed species. Instead, it is pointing to a link with arseniosiderite and yukonite.

It appears that the Ca/As ratios of the iron (III) oxyhydroxides in the process tailings are higher than their predecessors. Based on 212 microprobe analyses, Ca/As molar ratio of the iron (III) oxyhydroxides in 20 is 0.56 ± 0.02. This becomes 0.66 ± 0.02 and 0.61 ± 0.02 after cyanidation and SO_2/air processes, respectively and the variations are significant at 95% confidence.

3.2. Speciation and Molecular-Scale Characterization of Arsenic

Arsenic occurs exclusively as As^{5+} in the ore and tailings resulting from cyanidation and SO_2/air processes, as indicated by measurement of absorption edge positions on each calibrated As *K*-edge sample XANES spectrum (Fig. 5). The *K*-edge XANES spectra are otherwise practically identical and of little use for comparison of changes in As species as a function of different processing steps. Because the experimental tailings were dried following the cyanide leaching tests, XANES spectra may not be representative of any changes in speciation, which may have occurred during the experiments. Although there is no indication of the presence of reduced arsenic species in the XANES spectra, contributions from reduced species that make up less than 10% of the bulk spectra would be difficult to reconcile.

The k^3-weighted EXAFS spectra of the bulk samples are shown on Figure 6. The k^3-weighted EXAFS spectra of ORE and 22 are similar and resemble the arsenian goethite model compound. Sample 18, on the other hand, resembles the amorphous ferric arsenate model compound. The EXAFS spectrum of sample 20 appears to be a mixture of the As-goethite model

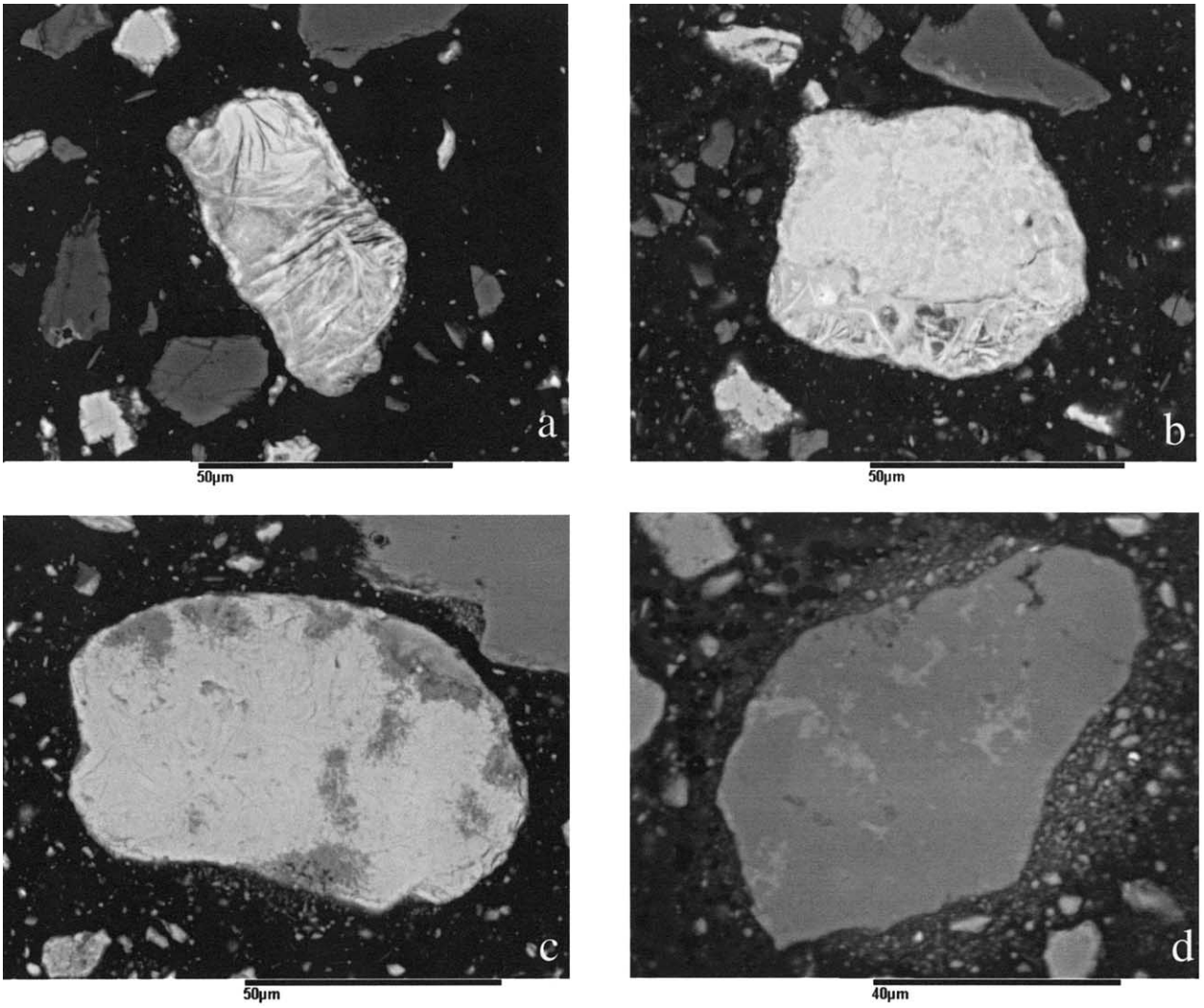

Fig. 2. Backscattered electron micrographs of (a) an arseniosiderite particle (sample 20-SO2); (b) a composite particle of arseniosiderite (upper portion of the grain displaying fuzzy heterogeneity) and pharmacosiderite (lower portion of the particle with lamellar-like features (sample 20); (c) an arseniosiderite particle (light grey) containing patches of jarosite-like phase (dark grey) (sample 22); (d) As-bearing jarosite (grey) with relict iron (III) oxyhydroxide grains (light grey) (sample 22).

and amorphous ferric arsenate model compound, based on visual comparison of the relevant EXAFS spectra.

Fourier transformation of the k^3-weighted frequencies produces partial radial structure functions which (when corrected for phase shift due to neighboring atoms) provide quantitative estimates of interatomic distances between the As atom and its nearest neighbors. The major peak in all the bulk EXAFS spectra centered at 1.3 Å corresponds to an As-O distance (Fig. 7). The samples display a second prominent peak at ~2.7 Å corresponding to an As-Fe distance and a third at ~3.3 Å corresponding to an As-Ca distance (all uncorrected for phase shift) in reference to model compounds such as scorodite, amorphous ferric arsenate, arseniosiderite and yukonite. Analysis of individual scans confirmed that both the As-Fe and As-Ca peaks are real as they are present in each scan at the same *R*-value and above the background ripples that are considered as the random noise. For instance, the variance of the As-Fe and As-Ca peaks in *R*-space was found to be less than 0.0005 Å for many samples. The random noise was defined as the mean Fourier transform magnitude plus 3 times the standard deviation in the 4 to 7 Å range. The Fourier transform magnitude of the As-Fe peaks are 1.5 to 3 times above this background value and it is ~1.3 to 3 times for the As-Ca peaks.

Because the bulk EXAFS spectra are weighted averages of all contributions from the As species present in the samples, interpretation of the bulk EXAFS spectra becomes ambiguous without the micro-EXAFS spectra of individual arsenate and iron (III) oxyhydroxide grains that make up the bulk spectra. Micro-EXAFS spectra (Fig. 8) of individual iron (III) oxyhydroxide grains with varying As concentrations from ~2 to 26% As_2O_5 (Table 4) indicate an As-Fe distance at ~2.7 Å (uncorrected for phase shift). Surprisingly, the peak at ~3.3 Å (uncorrected for phase shift) corresponding to the As-Ca distance on the bulk EXAFS spectra, is present in all the micro-EXAFS

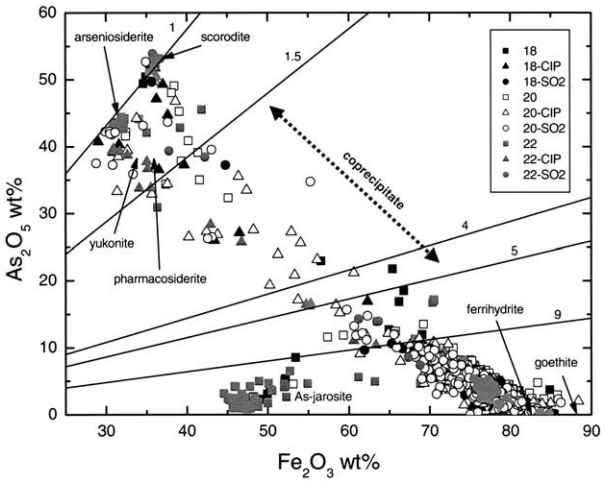

Fig. 3. Variation of As_2O_5 as a function of Fe_2O_3 in iron (III) oxyhydroxides, arsenates and jarosites. Arrows with mineral labels point to theoretical mineral compositions. Diagonal lines with numbers are Fe/As molar ratios.

spectra of iron (III) oxyhydroxides (Fig. 9). This peak, present in the bulk EXAFS spectra, was initially thought to have arisen from Ca-Fe arsenates. Its presence in the micro-EXAFS spectra of the iron (III) oxyhydroxides suggests that Ca occurs in close proximity to the adsorbed As in iron (III) oxyhydroxides.

The EXAFS fits of iron (III) oxyhydroxides, performed in *k*-space from 3 to 13 $Å^{-1}$ and employing 3 atomic shells (O, Fe and Ca) resulted in slight shifts in the second and third neighbor peaks of the fitted spectra to longer distances. Accordingly, a second As-Fe shell was added to the fit. This fit was still somewhat unsatisfactory; therefore, a shell arising from double scattering (i.e., multiple scattering) of photoelectrons within the arsenate tetrahedron was added along with the second As-Fe shell, resulting in marked improvements to the fits. The use of each shell in the fits is justified based on the estimated statistical parameters for goodness-of-fit for successive fits as per Thompson et al. (1997). The goodness-of-fit is the reduced chi squared value (ε^2), which differs from that of Stern et al. (1995) in the fitting space used:

$$\varepsilon^2 = \frac{N_{ind}}{(N_{ind} - p) \cdot n} \cdot \sum_{i=1}^{n} w_i(\chi_i^{\exp}(k) \cdot k^3 - \chi_i^{fit}(k) \cdot k^3)^2$$

where N_{ind} is number of independent data points, p is number of parameters floated in fits, n is number of experimental data points, w_i is weighting parameter, $\chi^{\exp}(k)$ and $\chi^{\text{fit}}(k)$ are the experimental and fitted EXAFS functions. N_{ind} is expressed as:

$$N_{ind} = \frac{2 \cdot \Delta k \cdot \Delta R}{\pi}$$

where Δk is the range in *k*-space and ΔR is the range in *R*-space used in fitting (Lytle et al., 1989; Stern, 1993; Stern et al., 1995). Because background subtraction removes information at low R, ΔR is defined as the range, over which there is real data (i.e., 0.8 Å as the starting *R*-value). We have assumed no weight (i.e., $w_i = 1$) for experimental measurements following the approach adopted by Thompson et al. (1997).

The Debye-Waller parameter for the multiple-scattering (MS) shell was fixed at 0 in the fits due to our inability to estimate a reasonable value for this parameter, which is a function of the disorder (i.e., Debye-Waller parameters) of neighboring shells. The fit-derived MS distances range from 3.10 −3.17 Å (Tables 5 and 6), which is within the range found

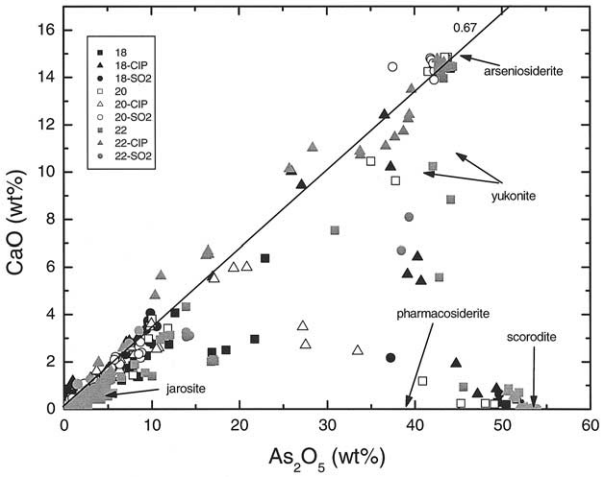

Fig. 4. CaO vs. As_2O_5 plot of iron (III) oxyhydroxides, arsenates and jarosites in the ore and cyanidation test samples. Arrows with mineral labels point to theoretical mineral compositions. The line corresponding to Ca/As molar ratio of 0.67 is shown as a reference.

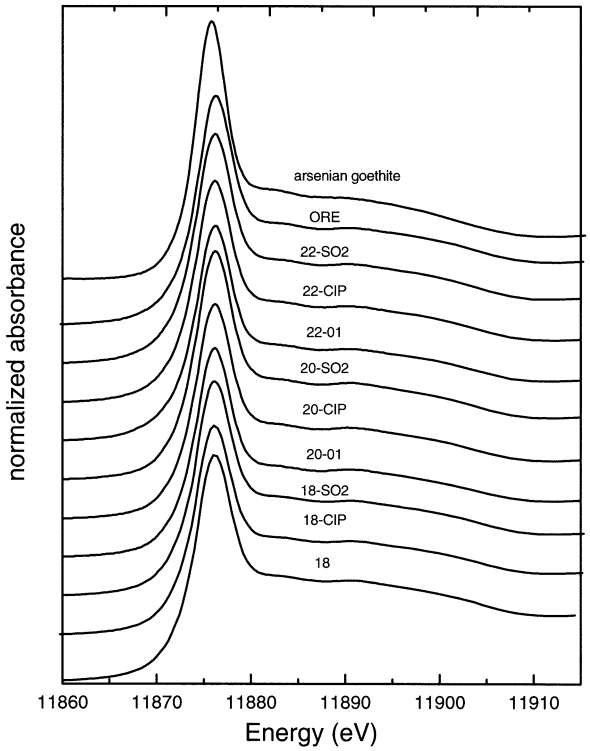

Fig. 5. As *K*-edge XANES spectra of bulk samples. XANES spectra of arsenian goethite (As(V)-bearing goethite) is shown for comparison of the edge positions.

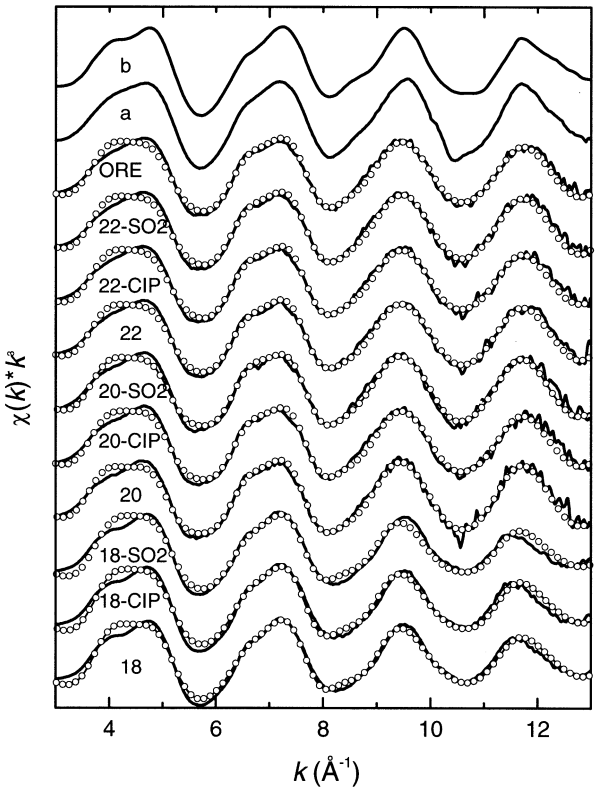

Fig. 6. k^3-weighted bulk EXAFS spectra. Unfiltered experimental spectra are shown by solid lines and the fitted spectra by circles. Inclusion of MS shell in the fits simulates the first oscillation feature at ~4.2 Å-1. Spectra of arsenian goethite (a) and amorphous ferric arsenate (b) are shown for comparison.

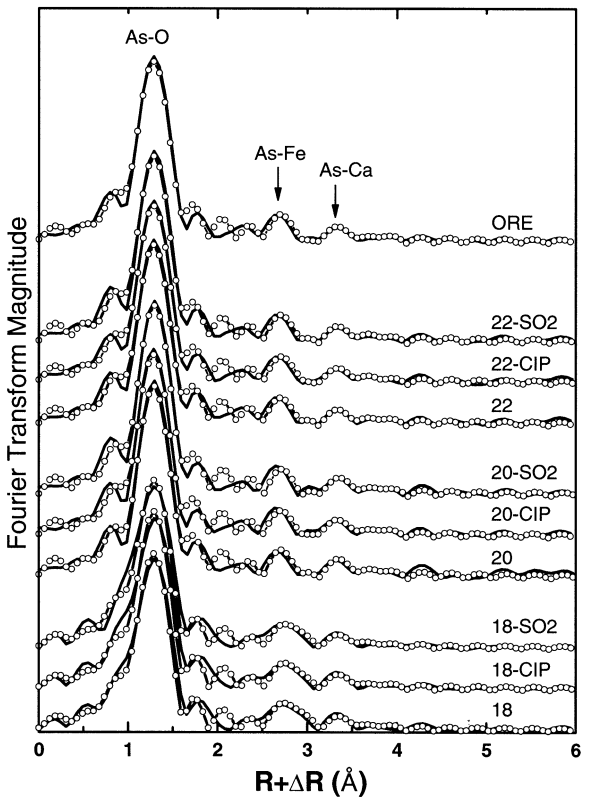

Fig. 7. Fourier-transformed bulk EXAFS spectra. Transformation performed within the *k* interval of 3 to 13 Å at 0.01 Å intervals. Radial distance not corrected for phase shift. Experimental curves are indicated by solid lines and the lines with circles are those of the fitted spectra.

by Foster (1999) for MS in the arsenate tetrahedron in the EXAFS spectrum of scorodite. The fit-derived coordination numbers for MS shells were between 18.8 and 25.7; these values are much higher than the maximum number of double-scattering paths (i.e., As-O-O-As) that can occur between an As atom and its four neighboring oxygen atoms in tetrahedral configuration, which is 12. As described by Paktunc et al. (2003), there are many possible reasons for the high coordination numbers in the MS shell fits. One of them is the choice of 0.85 as the value for S_0^2, representing shake-up and shake-off effects arising from the central As atom (Sayers and Bunker, 1988). The effect of S_0^2 on the coordination number of the MS shell was found to be limited. For instance, a change of S_0^2 by 0.1 causes the coordination number of the MS shell to vary about ± 2.5 that is within the estimated uncertainty value of about $\pm 20\%$ for the coordination numbers. The other alternatives include the choice of the specific MS path chosen to represent the other 11 MS paths (the number of degenerate paths varies with the As-O bond lengths in the tetrahedron) and minor contributions to the EXAFS spectrum that influence the amplitude of the peak attributed to MS but remain unaccounted for (Foster et al., 1998; Foster et al., 2003). Because of the rather unsatisfactory fit parameters for the MS shell and resulting lower coordination numbers for the As-Fe shell, we decided to exclude it in the fits despite the improvements in the fit quality and especially the fit over the first oscillation feature at ~4.2 $Å^{-1}$ (Figs. 6 and 8).

The As-O interatomic distance is 1.69 Å for the bulk EXAFS and micro-EXAFS of the iron (III) oxyhydroxides (Tables 5 and 6). Along with the coordination numbers ranging from 4.57 to 5.35 for the bulk EXAFS and from 4.01 to 4.84 for the micro-EXAFS, this suggests tetrahedral coordination of first shell oxygen atoms around a central As atom. The deviation of the As-O coordination numbers from the nominal value of 4 is within the uncertainty value of ± 1.7 determined by comparing the experimental data of scorodite and arseniosiderite against the nominal structural parameters. The uncertainty value of the As-O radial distance is ± 0.01 Å.

The As-Fe distances are in the range of 3.29 to 3.34 Å for the bulk EXAFS spectra. Corresponding coordination numbers range from 1.87 to 3.11. It was possible to fit a second As-Fe shell to some of the bulk EXAFS spectra with interatomic distances ranging from 2.79 to 2.86 Å. Coordination numbers of this second As-Fe shell range from 0.50 to 1.01. However, the addition of this second As-Fe shell did not improve the quality of fit. Uncertainties in the coordination numbers and radial distances for the As-Fe shell as determined by comparing the experimental data of scorodite and arseniosiderite against their nominal structural parameters and the highest standard deviations in the fits at 95% confidence limit are ± 0.4 and ± 0.03 Å for the bulk EXAFS. The As-Fe distances of iron (III)

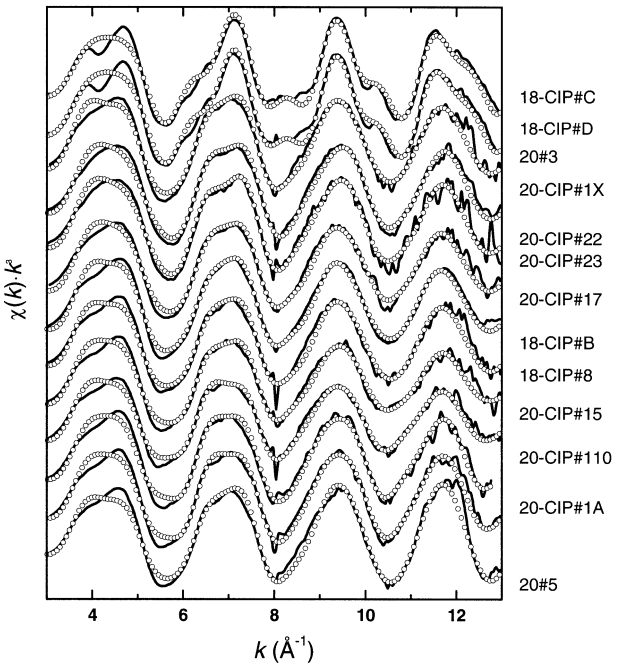

Fig. 8. k^3-weighted micro-EXAFS spectra of iron (III) oxyhydroxide and arsenate mineral particles. Experimental spectra are unfiltered and indicated by solid lines and the fitted spectra by circles. Inclusion of MS shell in the fits simulates the first oscillation feature at ~4.2 Å-1 for iron (III) oxyhydroxide spectra.

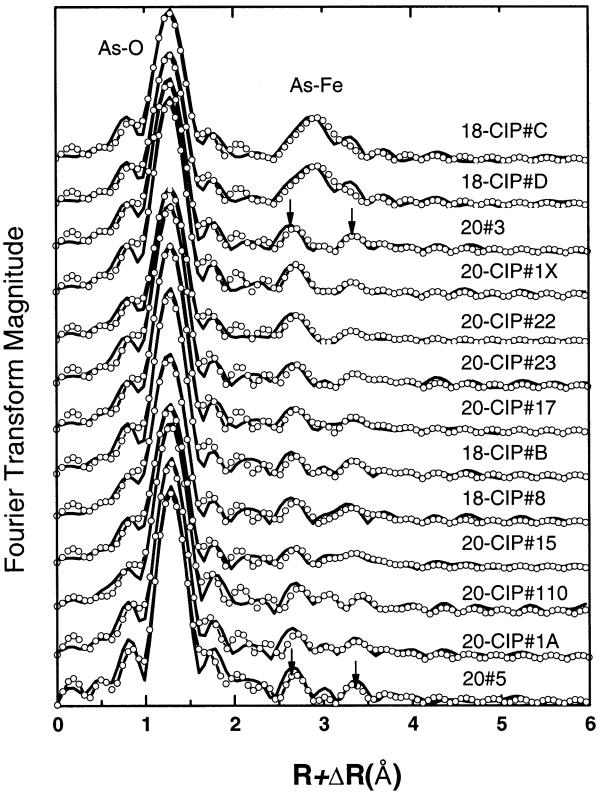

Fig. 9. Fourier-transformed micro-EXAFS spectra of iron (III) oxyhydroxide and arsenate mineral particles. Transformation performed within the *k* interval of 3 to 13 Å at 0.01 Å intervals. Radial distance not corrected for phase shift. Experimental curves are indicated by solid lines and the lines with circles are those of the fitted spectra. Arrowhead on the left point to As-Fe shell and the one on the right point to As-Ca shell.

oxyhydroxides by micro-EXAFS range from 3.24 to 3.32 Å and are similar to the distances defined by Waychunas et al. (1993) for the bidentate-binuclear geometry. With the exception of one, the values near the lower end of this range are from iron (III) oxyhydroxides containing lower As concentrations whereas iron (III) oxyhydroxides with higher As (i.e., 6 to 26% As_2O_5) tend to have As-Fe radial distances gathering around 3.28 Å. Similar to the bulk EXAFS, it was possible to fit a second shell As-Fe distances to some of the spectra without an improvement in the fit quality. This second shell As-Fe distances are between 2.80 and 2.90 Å with an median value of 2.82 Å. The median value is comparable to the distances proposed by Manceau (1995) and Fendorf et al. (1997), and slightly smaller than those of Randall et al. (2001) for the edge-sharing or bidentate-mononuclear complex. With the inclusion of a MS shell in the fits, the As-Fe distances for the second As-Fe shell become shorter (i.e., 2.66–2.68 Å for the bulk EXAFS and 2.66 to 2.70 Å for the micro-EXAFS).

The As-Ca interatomic distances are relatively uniform varying from 4.14 to 4.19 Å for the bulk EXAFS and micro-EXAFS of iron (III) oxyhydroxides (Tables 5 and 6), and similar to the As-Ca interatomic distances obtained from micro-EXAFS analysis of single grains of arseniosiderite but slightly shorter than the experimentally determined 4.24 Å and 4.21 Å distances for the arseniosiderite and yukonite model specimens (Paktunc et al., 2003). The coordination numbers vary from 4.33 to 6.04 for the bulk EXAFS and from 2.62 to 5.69 for the micro-EXAFS of iron (III) oxyhydroxide grains. Uncertainties in the coordination numbers and radial distances as determined by comparing the experimental data of arseniosiderite against its nominal structural parameters and the highest standard deviations in the fits at 95% confidence limit are ± 1.6 and ± 0.03 Å. A fixed Debye-Waller parameter of 0.017 was used for some samples where fitting resulted in unrealistically high coordination numbers (i.e., 7.3 to 8.3) for the Ca shell. The use of 0.017 as the fixed Debye-Waller parameter for the Ca shell of atoms is justified because it is consistent with the values obtained from arseniosiderite and yukonite. The Debye-Waller parameter ranged from 0.0112 to 0.0205 for the cases where it was allowed to float (Tables 5 and 6). Contribution of Ca shells to the fits is approximately 2 to 3%. This is comparable to the Fe contributions in some instances and supports the presence of Ca scatterers in addition to the significance tests discussed above.

It was originally considered by Paktunc et al. (1996, 2000) that Ca occurred as adsorbed species on iron (III) oxyhydroxide surfaces. However, the presence of Ca atoms around As in iron (III) oxyhydroxides as indicated by micro-EXAFS spectroscopy cannot be explained by pure adsorption. Instead, this relationship suggests coprecipitation of Ca with As on the surfaces of iron (III) oxyhydroxides. The Ca-As interatomic distance is similar to the distance obtained from the micro-EXAFS analysis of single grains of arseniosiderite (Table 6). Arseniosiderite and yukonite model specimens analyzed in bulk at the Stanford Synchrotron Radiation Laboratory have

Table 5. EXAFS fitting results summarizing the local coordination environment around a central arsenic atom (within 3–13 $Å^{-1}$).[a]

	As-O			As-Fe			As-Ca				
Sample	CN	R (Å)	σ^2 ($Å^2$)	CN	R (Å)	σ^2 ($Å^2$)	CN	R (Å)	σ^2 ($Å^2$)	E_0 (eV)	$\Delta\chi^2$
18	5.35	1.69	0.0034	2.96	3.34	0.0110	4.87	4.17	0.017*	−3.71	0.039
18-CIP	5.34	1.69	0.0033	2.17	3.34	0.0091	4.67	4.18	0.017*	−3.50	0.049
18-SO2	5.29	1.69	0.0037	2.12	3.34	0.0094	4.33	4.19	0.017*	−3.00	0.057
20	4.68	1.69	0.0015	2.23	3.30	0.0109	6.03	4.16	0.017*	−7.50	0.038
20-CIP	4.83	1.69	0.0022	1.87	3.29	0.0100	5.67	4.16	0.017*	−6.20	0.043
20-SO2	4.65	1.69	0.0016	1.97	3.29	0.0111	5.68	4.17	0.017*	−5.83	0.039
22	4.57	1.69	0.0018	3.11	3.29	0.0141	5.98	4.17	0.0205	−6.35	0.037
22-CIP	4.75	1.69	0.0022	2.31	3.29	0.0112	4.52	4.17	0.017*	−6.55	0.036
22-SO2	4.60	1.69	0.0017	2.69	3.29	0.0129	5.65	4.17	0.0198	−6.31	0.036
ORE	4.79	1.69	0.0021	2.65	3.29	0.0123	6.04	4.16	0.0205	−6.44	0.034

[a] CN: coordination number; R: interatomic distance; σ^2: Debye-Waller parameter; E_0: energy offset;

* fixed value; $\Delta\chi^2$: error parameter, $\Delta\chi^2 = \sum_{i=1}^{n}(\chi_i^{exp}(k)\cdot k^3 - \chi_i^{fit}(k)\cdot k^3)^2 / \sum_{i=1}^{n}(\chi_i^{exp}(k)\cdot k^3)^2$;

Uncertainties in CN values: ±1.7 for As-O, ±0.4 for As-Fe and ±1.5 for As-Ca; in R values: ±0.01 A for, As-Fe and ±0.03 Å for As-Ca estimated by comparing the EXAFS analysis of a scorodite and arsenioside nominal crystal structure parameters (R and CN for scorodite, and CN for arseniosiderite), and/or highest deviations in the fits at 95% confidence limit.

slightly longer (i.e., ~0.08 Å) As-Ca interatomic distances (Paktunc et al., 2003). The coordination numbers that are mostly in the 4 to 5 range are compatible with a coprecipitate having local structure similar to that of arseniosiderite. In arseniosiderite structure, an arsenate tetrahedron shares its three oxygens with three Fe-O octahedra linked at the corners to form a ring-like structure (Fig. 10) or edge and corner-linked octahedra forming one portion of the central girdle of the Keggin-like molecule. There are three Ca-O polyhedra surrounding the arsenate tetrahedron in edge-shared arrangement with the Fe-O octahedra below. There is an additional Ca-O polyhedron making the total number of Ca atoms 4 around the arsenate tetrahedron. Thus, it appears in essence a nanocluster of arseniosiderite or similar structure can be built upon a bidentate-binuclear arsenate complex on iron (III) oxyhydroxide as a coprecipitate. It is conceivable then the variation in the As-Fe interatomic distances of iron (III) oxyhydroxides is due to contributions from the coprecipitate as well as the bidentate-binuclear arsenate. The discovery of Ca-Fe coprecipitate would also explain the strong As-Ca correlations in iron (III) oxyhydroxides having As/Ca ratios identical to that of arseniosiderite (Fig. 4).

The best fit to the bulk EXAFS spectrum of samples 18, 18-CIP and 18-SO2 indicates an interatomic distance of 3.34 Å between the central As atom and Fe, which are the weighted averages of all the As minerals present in the sample. Coordi-

Table 6. Micro-EXAFS fitting results summarizing the local coordination environment around a central arsenic atom mineral grains (fitting in *k*-space within 3–13 $Å^{-1}$).[a]

		As-O			As-Fe			As-Ca				
Sample		CN	R (Å)	σ^2 ($Å^2$)	CN	R (Å)	σ^2 ($Å^2$)	CN	R (Å)	σ^2 ($Å^2$)	E_0 (eV)	$\Delta\chi^2$
20 #5	2% As_2O_5	4.01	1.69	0.0004	2.58	3.28	0.0133	5.04	4.14	0.017*	−10.0	0.035
20-CIP #1A	3% As_2O_5	4.51	1.69	0.0017	0.71	3.24	0.0046	5.69	4.16	0.017*	−8.68	0.037
20-CIP #110	3% As_2O_5	4.46	1.69	0.0019	0.39	3.25	0.0006	5.10	4.17	0.0168	−8.17	0.037
20-CIP #15	3% As_2O_5	4.56	1.69	0.0031	0.72	3.25	0.0054	5.63	4.14	0.017*	−9.47	0.040
18-CIP #8	6% As_2O_5	4.82	1.69	0.0033	1.14	3.27	0.0077	5.09	4.15	0.017*	−9.6	0.046
18-CIP #B	8% As_2O_5	4.52	1.69	0.0021	2.15	3.30	0.0147	5.25	4.15	0.017*	−8.9	0.046
20-CIP #17	20% As_2O_5	4.80	1.69	0.0025	2.44	3.32	0.0137	4.97	4.16	0.017*	−7.67	0.017
20-CIP #23	26% As_2O_5	4.71	1.69	0.0026	2.31	3.28	0.0142	2.62	4.17	0.0112	−7.2	0.040
18-CIP #C	scorodite	3.64	1.68	0.0015	2.50	3.36	0.0044				−8.5	0.042
18-CIP #D	scorodite	4.31	1.68	0.0016	2.82	3.36	0.0048				−8.6	0.039
20 #3	arseniosiderite	4.58	1.69	0.0024	3.60	3.29	0.0165	5.53	4.14	0.0175	−10.0	0.038
20-CIP #1X	arseniosiderite	4.74	1.69	0.0021	2.11	3.24	0.0092	3.60	4.15	0.0168	−8.6	0.034
20-CIP #22	arseniosiderite	3.57	1.69	0.0021	2.44	3.26	0.0116	2.44	4.17	0.0146	−8.2	0.049

[a] CN: coordination number; R: interatomic distance; σ^2: Debye-Waller parameter, E_0: energy offset; ∗ fixed value; $\Delta\chi^2$: error parameter as per Table 5; uncertainties in CN values: ±0.7 for As-O, ±1.5 (scorodite and arseniosiderite) ±0.4 (iron (III) oxyhydroxides) for As-Fe and ±1.6 for As-Ca; in R values: ±0.00 Å for As-O, ±0.03 Å for As-Fe and ±0.03 Å for As-Ca estimated by comparing the micro-EXAFS analyses of scorodite and arseniosiderite to their nominal crystal structure parameters (R and CN for scorodite; CN for arseniosiderite), and/or the highest standard deviations in the fits at 95% confidence limit; corresponding electron microprobe analyses are listed in Table 4.

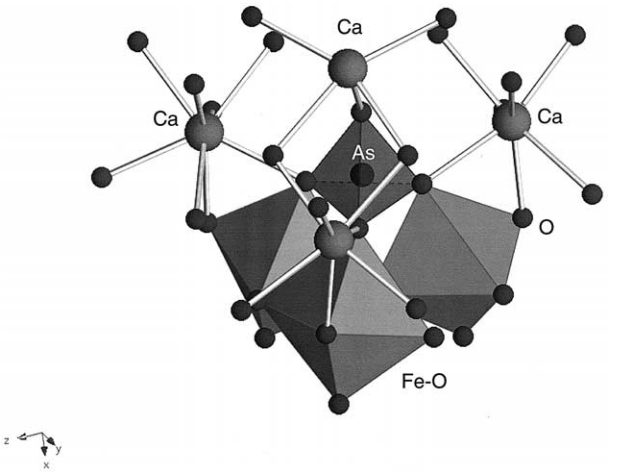

Fig. 10. Schematic representation of a cluster around an arsenate tetrahedron in arseniosiderite structure. Arsenate tetrahedron is corner-linked to three Fe-O octahedra and four Ca-O polyhedra.

nation numbers were estimated to be between 2.12 and 2.96. The As-Fe distances in the 20 and 22 sets of samples are shorter (i.e., 3.29–3.30 Å). Coordination numbers for this shell of Fe atoms range from 1.87 to 3.11. The As-Fe interatomic distances are slightly shorter than the As-Fe distance of 3.36 Å in scorodite and 3.37 Å in amorphous ferric arsenate, and slightly longer than the As-Fe distance of 3.24–3.26 Å for the bidentate-binuclear arrangement in iron (III) oxyhydroxides. The monodentate-mononuclear arrangement results in an As-Fe radial distance of 3.60 Å. The As-Fe distance is approximately 3.2 Å in arseniosiderite. It appears that the bulk spectra are representing a mixture of bidentate-binuclear complexes on iron (III) oxyhydroxides, ferric arsenates and Ca-Fe arsenates. Fitting of the third peak on the Fourier-transformed EXAFS spectra at ~3.3 Å (uncorrected for phase shift) resulted in As-Ca interatomic distances of 4.17, 4.18 and 4.19 Å for samples 18, 18-CIP and 18-SO2. The values range from 4.16 to 4.17 Å for the other samples. Coordination numbers for this shell range from 4.3 to 6.0. The distances are comparable with the As-Ca interatomic distances obtained from micro-EXAFS analysis of single grains of iron (III) oxyhydroxides and arseniosiderite.

These results are similar to the Ketza River mine tailings subjected to column-leaching studies (Paktunc et al., 2003). With the exception of the discovery of a Ca shell in this study, the results are supportive of the findings of Waychunas et al. (1993, 1995, 1996) and Fendorf et al. (1997) in that arsenate occurs predominantly as inner-sphere bidentate complexes on iron (III) oxyhydroxide surfaces. The As-Fe distances are suggestive of the predominant presence of bidentate-binuclear or corner-linking arsenate complexes with minor bidentate-mononuclear or edge-sharing arsenate complexes on iron (III) oxyhydroxide surfaces.

On average, iron (III) oxyhydroxides with Fe/As molar ratios greater than 4 accommodated 0.016 mol As and 0.012 mol Ca per mole of Fe. Iron (III) oxyhydroxides with Fe/As molar ratios less than 4, on the other hand, accommodated up to 0.625 mol As and 0.4 mol Ca per mole of Fe. Singly-coordinated reactive surface sites on a small unit of goethite structure

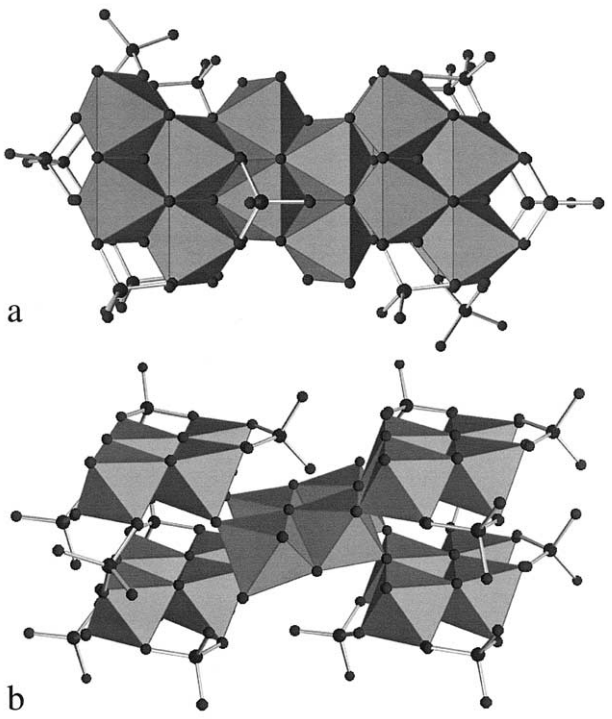

Fig. 11. Polyhedral representation of a small unit of goethite structure with bidentate-binuclear arsenate tetrahedra (shown in ball and stick representation) attached to singly coordinated sites. Goethite structure in this illustration is composed of 20 Fe-O(OH) octahedra; (a) viewed on the (001) surface; (b) oblique view towards the (010) surface.

consisting of 20 Fe-O(OH) octahedra include 28 oxo (as per IUPAC nomenclature for Fe-O surface sites) and 10 hydroxo (Fe-OH) sites. Up to 6 bidentate-binuclear arsenate can be accommodated on oxo-oxo sites located on the (100) and (001) surfaces and up to 8 bidentate-binuclear arsenate on hydroxo-oxo sites on the (010) surfaces (Fig. 11). This combination leaves only four surface sites on the (010) surfaces for attachment by 2 bidentate-mononuclear arsenate complexes. These correspond to maximum adsorption densities of 1.1 arsenate per nm^2 on (100) and (001) surfaces, and 1.5 arsenate per nm^2 on (010) surfaces. The As/Fe molar ratio resulting from the combined maximum adsorption densities is 0.7. This value is identical to the experimentally determined arsenate saturation level of Fuller et al. (1993). Maximum adsorption is possible with the bidentate-binuclear and bidentate-mononuclear attachments, because these adsorption geometries do not result in the accumulation of surface charges. The presence of high As-bearing iron (III) oxyhydroxides (i.e., $\sim <$ 0.625 mol As per mole of Fe in this case) can be explained by the formation of nanoparticles due to inhibition of growth by adsorption of bidentate-binuclear arsenate complexes in all directions. Manceau (1995) argued that particle growth along Fe-O chains could only be inhibited by bidentate-mononuclear complexes. As indicated above and in accordance with Waychunas et al. (1995), bidentate-binuclear arsenate complexes can effectively poison almost all the available growth sites in all directions. The reason for the increased levels of As and Ca in iron (III) oxyhydroxide is probably related to the timing of adsorption in

Table 7. Distribution of arsenic estimated by least squares fitting of the smoothed EXAFS spectra to model compounds.[a]

	18	18-CIP	18-SO2	20	20-CIP	20-SO2	22	22-CIP	22-SO2
FeOxh 2%	—	—	—	36.2	23.5	42.7	39.6	23.4	43.2
FeOxh 20%	17.0	8.6	15.2	14.8	29.7	5.8	4.2	30.2	—
Arseniosiderite	—	27.9	27.8	10.2	3.4	18.5	10.9	9.4	15.3
Scorodite	3.7	8.7	3.0	15.0	0.3	4.9	2.3	0.7	1.6
Am.Fe.arsenate	79.4	54.8	54.0	23.8	43.1	28.1	43.0	36.3	39.9
Total	100.1	100.0	100.0	100.0	100.0	100.0	100.0	100.0	100.0
rss	545	652	690	223	164	177	149	135	134

[a] Fitting was performed within the *k*-range of 3–13 $Å^{-1}$ using LSFitXAFS (which is provided as an Electronic Annex); rss: residual sum of squares; FeOxh 2%: 20 #5; FeOxh 20%: 20-CIP #17 as listed on Table 6.

relation to iron (III) oxyhydroxide precipitation. Iron (III) oxyhydroxide precipitated earlier may not adsorb as much because of the use of the adsorption sites for cross-linkages of Fe polymer chains as originally suggested for As adsorption by Waychunas et al. (1993, 1996) and Fuller et al. (1993). It appears based on the preceding discussion that the iron (III) oxyhydroxides with high As and Ca concentrations probably represent clusters of iron (III) oxyhydroxide nanoparticles, coprecipitated with arsenates.

3.3. Behavior of Arsenic during Processing and Implications for Mobility

Cyanidation tests caused the release of varying concentrations of As into the solution. Arsenic releases of 6.6 and 4.7 mg/L resulted during cyanidation of samples 18 and 20, which contained 3.37 and 2.26 wt% As, respectively. Sample 22, on the other hand, released only 2.8 mg/L As to the supernatant solution. The SO_2/air cyanide destruction process caused higher As releases to the supernatant solution of sample 18 (i.e., 11.4 mg/L) whereas As levels in the supernatant solution were lower (2.4 and 1.1 mg/L) for samples 20 and 22, respectively. There are no striking differences in the identity or relative abundance of arsenate minerals among the samples to account for the above differences in As releases.

Radial distances between the main shell of Fe atoms and the central As absorber derived from fits to the bulk EXAFS spectra of samples of 20 and 22 are longer than that expected for a bidentate- binuclear As sorption geometry but are similar to As-Fe interatomic distances in Ca-Fe arsenates (i.e., arseniosiderite and yukonite) and in iron (III) oxyhydroxides with high As. Bulk EXAFS spectra of sample 18, which experienced the highest As releases, are different from the other samples. The differences are due to the presence of longer As-Fe radial distances in sample 18. With the consideration that the As-Fe interatomic distances obtained from the model scorodite and amorphous ferric arsenate compounds are 3.36 and 3.37 Å, the longer As-Fe distances in sample 18 are most likely to be the result of higher abundances of ferric arsenates in the sample. An estimate of the distribution of the As carriers was made by fitting the experimental k^3-weighted and smoothed EXAFS spectra to the model compounds of iron (III) oxyhydroxides, scorodite, amorphous ferric arsenate and arseniosiderite. Distribution of As among the As-carriers on weight percent basis is given in Table 7. The residual sum of squares listed on the table provides a measure of the goodness of the fit. The total values, which are not constrained in the fits, also indicate that the fit results are good. The uncertainties in the estimated mineral quantities due to errors associated with the determination of $\chi(k)$ values were estimated to be less than 19% based on variations in the replicate EXAFS spectra from several samples (Paktunc et al., 2003). Low As bearing iron (III) oxyhydroxides carry between 23 to 43% of the total As in samples 20 and 22. Sample 18 and its process tailings are distinctly different in that the amorphous ferric arsenate is determined to be a significant As carrier via this analysis. The lower bulk Fe/As ratio of this sample (Table 1) supports the presence of higher abundances of ferric arsenates. Higher As releases experienced by sample 18 during processing could then be attributed to this mineralogical difference, which could not be detected via X-ray diffraction and electron microprobe analysis.

Sustained alkaline conditions during cyanidation probably promoted the measured As releases. Maximum arsenate adsorption onto amorphous iron hydroxide and goethite occurs at pH 4 (Pierce and Moore, 1982; O'Reilly et al., 2001); thus, desorption of arsenate is favored under high-pH conditions (e.g., Smedley et al., 2002). In the pH range of 7.5 to 9, arsenate adsorption increases in a nearly linear relationship with decreasing pH (Fuller et al., 1993). In the case of 18-CIP, the pH remained alkaline until the end of SO_2/air process, thereby causing continued As release to the solution. Bulk As losses during cyanidation of sample 20 constitute only 0.023% of the total As present in the sample. This is reduced to 0.012% during the SO_2/air process. Ca/As molar ratio of the iron (III) oxyhydroxides with Fe/As molar ratios greater than 4 increased from 0.56 ± 0.02 to 0.66 ± 0.02 after cyanidation process. This increase is probably due to the high pH of 10.5 maintained during the process. The ratio decreased to 0.61 ± 0.02 after the SO_2/air process, which required a lower pH of 8.2. As the pH dropped to more neutral conditions, the process may have reversed with decreased OH^- in solution and promoted adsorption of As onto iron (III) oxyhydroxide surfaces. The increase in the Ca/As ratio of iron (III) oxyhydroxides following cyanidation could be due to desorption of As from iron (III) oxyhydroxides at high pH. The decrease following SO_2/air process could be explained by the dissolution of Ca-Fe arsenates coprecipitated with iron (III) oxyhydroxides.

In addition to adsorption/desorption reactions, dissolution of iron (III) oxyhydroxides would contribute to As releases. Changes in the surface charge resulting from attachment of H^+, OH^- or ligands to surface sites would influence the dissolution rates of iron (III) oxyhydroxides. For instance, the rate in-

creases with increases in both the negative surface charge and pH (Stumm and Morgan, 1996). In the case of binuclear attachment of arsenate ions, total net surface charge does not increase; therefore, release of As by proton- or ligand-promoted dissolution of the host is unlikely. Furthermore, due to high activation energy requirements in the detachment of two metal centers for binuclear surface complexes (Biber et al., 1994), dissolution of the host iron (III) oxyhydroxides is expected to be retarded by binuclear attachment of arsenate complexes. Reductive dissolution of iron (III) oxyhydroxides, which is much faster than ligand- or proton-promoted dissolution, should be taken into consideration for disposal options utilizing thick water covers.

According to Robins (1987), ferric arsenates are regarded as thermodynamically unstable in neutral and basic environments. On the contrary, ferric arsenate compounds having Fe/As molar ratios that are greater than 4 are considered to be stable (Krause and Ettel, 1985, 1989; Harris, 2000) and the preferred form of the precipitate from process solutions destined for disposal. Solubility of ferric arsenate compounds decreases with increasing Fe/As ratios (Krause and Ettel, 1989). For instance, while ferric arsenates with Fe/As ratios of ~2 have a solubility value of 7 mg/L As, those with Fe/As ratios of ~16 have less than 0.05 mg/L As solubility at pH 5 and 25°C (Krause and Ettel, 1989). Ca-Fe arsenates have higher solubilities (Swash and Monhemius, 1995). For instance, a solubility value of ~7 mg/L As at pH 6.8 and 25°C was reported for arseniosiderite by Krause and Ettel (1989).

Ferric arsenates, Ca-Fe arsenates and iron (III) oxyhydroxides with Fe/As molar ratios of less than 4 are significant As carriers in the process tailings destined for the tailings impoundment; therefore, continued high As releases are likely to occur from the tailings. Treatment of water in the tailings impoundment will be required to perpetuity before discharge into the environment. Furthermore, the speciation and chemical characteristics of As are similar in ore, tailings and process samples; therefore, mobilization of As from natural sources adjacent to the mine (e.g., unmined ore and mineralized rocks) and contamination of groundwater and surface waters from surface exposures and near surface ore are also possible and should be included in assessments.

4. CONCLUSIONS

Iron (III) oxyhydroxides with variable As concentrations from trace to ~34 wt% As_2O_5 form the most abundant As carriers in the Ketza River ores and their process tailings with lesser quantities of scorodite, arseniosiderite, yukonite, and other ferric and Ca-Fe arsenates. In addition, As occurs in jarosite and pharmacosiderite in minor to trace quantities. Iron (III) oxyhydroxides also contain variable Ca concentrations which correlate well with As and the variation appears to be controlled by arseniosiderite composition.

XANES spectra indicate that As occurs exclusively as As^{5+} in the ores and process tailings. Micro-EXAFS spectra of individual iron (III) oxyhydroxide grains with varying As concentrations from ~2 to 26% As_2O_5 specify As-Fe interatomic distances of 3.24 to 3.32 Å. These correspond to the corner-linking or bidentate-binuclear arsenate complexes. In addition, some of the samples appear to possess a second Fe shell at a shorter distance varying from 2.80 to 2.90 Å, which correspond to edge-sharing or bidentate-mononuclear arsenate complex. The lower end of the dominant As-Fe distances (i.e., 3.24 Å) is representing iron (III) oxyhydroxides containing 3 wt% As_2O_5. The higher end of the range, with one exception, represents iron (III) oxyhydroxides with higher As (i.e., 6 to 26% As_2O_5). It appears that the availability and coprecipitation of arsenate during iron (III) oxyhydroxide crystallization gave rise to the wide range of As concentrations observed in iron (III) oxyhydroxides, probably as a function of particle size with nanocrystals representing those with high As.

The As-Ca interatomic distances gather around 4.14 to 4.17 Å and are similar to the As-Ca interatomic distances obtained from micro-EXAFS analysis of single grains of arseniosiderite. The presence of Ca scatterers around As in the iron (III) oxyhydroxides and the strong As-Ca correlations in iron (III) oxyhydroxides point to a coprecipitation origin rather than adsorption. Ca-Fe arsenates coprecipitated with iron (III) oxyhydroxides are probably in the form of nanoclusters or small crystallites.

Fits to the EXAFS spectra of the bulk samples (which represents the weighted averages of all the As species present) indicate that the samples are dominated by bidentate-binuclear attachment of arsenate ions onto iron (III) oxyhydroxides with contributions from ferric arsenates and Ca-Fe arsenates. Similar to the micro-EXAFS results, the As-Ca interatomic distances and coordination numbers of the bulk EXAFS spectra are essentially due to discrete grains of arseniosiderite and an arseniosiderite-like coprecipitate in iron (III) oxyhydroxides. Covariation of Ca with As in iron (III) oxyhydroxides as determined by electron microprobe analysis supports the coprecipitate origin for the presence of Ca in iron (III) oxyhydroxides.

In bench-scale processing of ore samples designed to mimic the large-scale processing, higher As releases were measured from the samples having longer bulk As-Fe radial distances. This finding is consistent with a greater abundance of soluble ferric arsenate minerals in these samples. Sustained alkaline conditions during the cyanidation step of the bench-scale processing probably promoted As desorption. The presence of highly soluble Fe and Ca-Fe arsenate minerals and relatively unstable iron (III) oxyhydroxides with Fe/As molar ratios of less than 4 in the process tailings suggests that the tailings in the impoundment will continue to release As. There is also the potential for mobilization of As from the natural sources in the near vicinity such the unmined ore and surrounding mineralized rocks and contamination of groundwater is likely.

Acknowledgments—Patricio Riveros and Guy Deschênes provided help with the bench-scale cyanidation and SO_2/air processes. Glenn Poirier and John Wilson provided supplementary electron microprobe analyses, wavelength-dispersive X-ray maps and XRD analyses. John Dutrizac and Allen Pratt reviewed the manuscript. Constructive comments from Dr. Donald Sparks (Associate Editor) and three anonymous journal referees were useful in the improvement of the manuscript. The project was funded in part by the Environmental Protection Branch of Environment Canada and Natural Resources Canada's synchrotron research initiative. Bulk XAFS experimental work was carried out at the Stanford Synchrotron Radiation Laboratory, a national user facility operated by Stanford University on behalf of the U.S. Department of Energy, Office of Basic Energy Sciences. Micro-XAFS experiments at the Pacific Northwest Consortium–Collaborative Access Team's (PNC-CAT) beamline at the Advanced Photon Source (APS) in Argonne was supported by the Natural Sciences and Engineering Research Council of Canada through a major facilities access grant.

Research at the PNC-CAT beamline, Advanced Photon Source, Argonne National Laboratory is also supported by the US Department of Energy under contracts W-31-109-Eng-38 (APS) and DE-FG03-97ER45628 (PNC-CAT).

Associate editor: D. L. Sparks.

REFERENCES

Biber M. V., Dos Santos Afonso M., and Stumm W. (1994) The coordination chemistry of weathering: IV. Inhibition of the dissolution of oxide minerals. *Geochim. Cosmochim. Acta* **58,** 1999–2010.

Devuyst E. A., Conard B. R., Vergunst R., and Tandi B. (1989) A cyanide removal process using sulfur dioxide and air. *J. Metall.* **1989 (December),** 43–45.

Fendorf S., Eick M. J., Grossl P., and Sparks D. (1997) Arsenate and chromate retention mechanisms on goethite. 1. Surface structure. *Environ. Sci. Technol.* **31,** 315–320.

Foster A. L. (1999) Partitioning and transformation of arsenic and selenium in natural and laboratory systems. Ph.D. thesis. Stanford University.

Foster A. L., Brown G. E. Jr., Tingle T. N., and Parks G. A. (1998) Quantitative arsenic speciation in mine tailings using X-ray absorption spectroscopy. *Am. Mineral.* **83,** 553–568.

Foster A. L., Brown G. E. Jr., and Parks G. A. (2003) X-ray absorption fine structure study of As(V) and Se(IV) sorption complexes on hydrous Mn oxides. *Geochim. Cosmochim. Acta* **67,** 1937–1953.

Fuller C. C., Davis J. A., and Waychunas G. A. (1993) Surface chemistry of ferrihydrite: Part 2. Kinetics of arsenate adsorption and coprecipitation. *Geochim. Cosmochim. Acta* **57,** 2271–2282.

George G. N. and Pickering I. J. (1995) *EXAFSPAK: A Suite of Computer Programs for Analysis of X-ray Absorption Spectra*. Stanford Synchrotron Radiation Laboratory.

Harris G. B. (2000) The removal and stabilization of arsenic from aqueous process solutions: Past, present and future. In *Minor Elements 2000* (ed. C. A. Young), pp. 3–20. Society for Mining, Metallurgy and Exploration.

Harvey C. F., Swartz C. H., Badruzzaman A. B. M., Keon-Blute N., Yu W., Ahsraf Ali M., Jay J., Beckie R., Niedan V., Brabander D., Oates P. M., Ashfaque K. N., Islam S., Hemond H. F., and Ahmed M. F. (2002) Arsenic mobility and groundwater extraction in Bangladesh. *Science* **298,** 1602–1606.

Krause E. and Ettel V. A. (1985) Ferric arsenate compounds: Are they environmentally safe? Solubilities of basic ferric arsenates. In *Impurity Control and Disposal: Proceedings of the 15th Annual CIM Hydrometallurgy Meeting,* pp. 1–20. CIM.

Krause E. and Ettel V. A. (1989) Solubilities and stabilities of ferric arsenates. *Hydrometrics* **22,** 311–337.

Lytle F. W., Sayers D. E., and Stern E. A. (1989) Report of the international workshop on standards criteria in X-ray absorption spectroscopy. *Physica B* **158,** 701–722.

Manceau A. (1995) The mechanism of anion adsorption on iron oxides: Evidence for the bonding of arsenate tetrahedra on free $Fe(O, OH)_6$ edges. *Geochim. Cosmochim. Acta* **59,** 3647–3653.

Newville M. J. (2001) IFEFFIT: Interactive XAFS analaysis and FEFF fitting. *J. Synchrotron Rad.* **8,** 322–324.

O'Reilly S. E., Strawn D. G., and Sparks D. L. (2001) Residence time effects on arsenate adsorption/desorption mechanism on goethite. *Soil Sci. Soc. Am. J.* **65,** 67–77.

Paktunc A. D., Szymanski J., Lastra R. and Laflamme G. (1996) Mineralogical characterization of the Ketza River mine tailings. Report MMSL No. 96-016(CR). CANMET, Mining and Mineral Sciences Laboratories.

Paktunc A. D., Szymanski J., Lastra R., Laflamme G., Enns V., and Soprovich E. (1998) Assessment of potential arsenic mobilization from the Ketza River mine tailings, Yukon, Canada. In *Waste Characterization and Treatment* (ed. W. Petruk), pp. 49–60. Society for Mining, Metallurgy and Exploration.

Paktunc A. D., Laflamme J. H. G., Riveros P. A. and Deschenes G. (2000) Arsenic mineralogy and bench-scale cyanidation testwork on composite materials from the Ketza River mine site, Yukon. Report MMSL No. 2000-017(CR). CANMET, Mining and Mineral Sciences Laboratories.

Paktunc A. D., Foster A., and Laflamme J. (2003) Speciation and characterization of arsenic in Ketza River mine tailings using X-ray absorption spectroscopy. *Environ. Sci. Technol.* **37,** 2067–2074.

Pierce M. L. and Moore C. B. (1982) Adsorption of arsenite and arsenate on amorphous iron hydroxide. *Water Res.* **16,** 1247–1253.

Randall S. R., Sherman D. M., and Ragnarsdottir K. V. (2001) Sorption of As(V) on green rust ($Fe_4(II)Fe_2(III)(OH)_{12}SO_4 \cdot 3H_2O$) and lepidocrocite (. γ-FeOOH): Surface complexes from EXAFS spectroscopy. *Geochim. Cosmochim. Acta* **65,** 1015–1023.

Robins R. G. (1987) Arsenic hydrometallurgy. In *Arsenic Metallurgy Fundamentals and Applications* (eds. R. G. Reddy, J. L. Hendrix, and P. B. Queneau), pp. 215–247. TMS.

Sayers D. E. and Bunker B. A. (1988) Data Analysis. In *X-ray Absorption: Principles, Applications, and Techniques of EXAFS, SEXAFS and XANES* (eds. D. C. Koningsberger and R. Prins), pp. 211–253. Wiley.

Smedley P. L., Nicolli H. B., Macdonald D. M. J., Barros A. J., and Tullio J. O. (2002) Hydrogeochemistry of arsenic and other inorganic constituents in groundwaters from La Pampa, Argentina. *Appl. Geochem.* **17,** 259–284.

Soprovich E. A. (2000) Arsenic release from oxide tailings containing scorodite, Fe-Ca arsenates and As-containing goethites. In *Proceedings of the Seventh International Conference on Tailings and Mine Waste '00,* pp. 23–26. Balkema.

Stern E. A. (1993) Number of relevant independent points in X-ray-absorption fine-structure spectra. *Phys. Rev. B* **48,** 9825–9827.

Stern E. A. (2001) Avoiding some pitfalls in XAFS analysis (abstract). Presented at Advanced Methods and Tricks of EXAFS Data Modeling Workshop. Annual NSLS Users' Meeting.

Stern E. A., Newville M., Ravel B., Yacoby Y., and Haskel D. (1995) The UWXAFS analysis package: Philosophy and details. *Phys. B* **208/209,** 117–120.

Stumm W. and Morgan J. J. (1996) *Aquatic Chemistry: Chemical Equilibria and Rates in Natural Waters*. Wiley.

Swash P. M. and Monhemius A. J. (1995) Synthesis, characterization and solubility testing of solids in the Ca-Fe-AsO_4 system. In *Proceedings of the Sudbury'95 Conference on Mining and the Environment*(eds. T. Hynes and M. Blanchette), CANMET, Ottawa, pp. 17–28.

Thompson H. A., Brown G. E., and Parks G. A. (1997) XAFS spectroscopic study of uranyl coordination in solids and aqueous solution. *Am. Mineral.* **82,** 483–496.

Waychunas G. A., Davis J. A., and Fuller C. C. (1995) Geometry of sorbed arsenate on ferrihydrite and crystalline FeOOH: Re-evaluation of EXAFS results and topological factors in predicting sorbate geometry, and evidence for monodentate complexes. *Geochim. Cosmochim. Acta* **59,** 3655–3661.

Waychunas G. A., Rea B. A., Fuller C. C., and Davis J. A. (1993) Surface chemistry of ferrihydrite: Part 1. EXAFS studies of the geometry of coprecipitated and adsorbed arsenate. *Geochim. Cosmochim. Acta* **57,** 2251–2269.

Waychunas G. A., Fuller C. C., Rea B. A., and Davis J. A. (1996) Wide angle X-ray scattering (WAXS) study of "two-line" ferrihydrite structure: Effect of arsenate sorption and counterion variation and comparison with EXAFS results. *Geochim. Cosmochim. Acta* **60,** 1765–1781.

Zabinsky S. I., Rehr J. J., Ankudinov A., Albers R. C., and Eller M. J. (1995) Multiple scattering calculation of X-ray absorption spectra. *Phys. Rev. B* **52,** 2995–3009.